COMPARATIVE ANALYSIS OF MORPHOLOGICAL (MCSS) AND LEARNING-BASED (SPG) STRATEGIES FOR DETECTING SIGNAGE OCCLUSIONS ALONG TRANSPORTATION CORRIDORS

N. Pascucci[1], S.-Y. Shin[2], M. Hodaei[2], D. Dominici[1], A. Habib[2] *
[1] DICEAA, Department of Civil, Environmental Engineering and Architecture, University of L'Aquila, Via G Gronchi 18, 67100, L'Aquila, Italy– nicole.pascucci@graduate.univaq.it, donatella.dominici@univaq.it
[2] Lyles School of Civil Engineering, Purdue University, 550 Stadium Mall Dr., West Lafayette, IN 47907, USA – (shin337, mhodaei, ahabib) @purdue.edu

KEY WORDS: Mobile Mapping Systems (MMS), Light Detection and Ranging (LiDAR), Signage Detection, Signage Visibility, Multi-Class Simultaneous Segmentation (MCSS), Super Point Graph (SPG), Semantic Segmentation

ABSTRACT:
Signage visibility along transportation corridors is critical for drivers in terms of road safety, traffic flow, and enforcement. Traffic signs that are easy to recognize by drivers and autonomous vehicles can help in avoiding accidents and improve safety. Nowadays, Mobile Mapping Systems (MMS) equipped with LiDAR units can scan road network components and its surrounding environment at a normal driving speed while collecting accurate geospatial data. Most traffic signs have well-defined geometric characteristics (e.g., linear or planar features) which can be identified in the 3D LiDAR data acquired by MMS. Therefore, MMS LiDAR data are an ideal source to recognize traffic signs. In addition to traffic sign detection, MMS can also identify vegetation along the right-of-way and evaluate signage visibility. Thus, this paper presents a framework for using MMS LiDAR data for traffic sign and vegetation detection which is a prerequisite for signage visibility analysis. For signage and vegetation detection, two alternative strategies are adopted: 1) a morphological approach and 2) a learning-based approach. For the geometric/morphological approach, Multi-Class Simultaneous Segmentation (MCSS) is utilized in this study. As for the learning-based strategy, semantic segmentation of LiDAR data are performed using Super Point Graph (SPG). Lastly, signage visibility analysis is conducted based on the occlusion rate assessed from different driver's viewpoints.

1. INTRODUCTION

Recent studies have shown that improving sign visibility will enhance driver awareness, reduce driver errors, and improve better compliance with traffic regulations (Smith et al., 2016; Oviedo-Trespalacios et al., 2019). These findings highlight the significance of proper signage visibility as a fundamental component of road infrastructure management and safety assessment (Babić et al. 2022). Recognized traffic signs not only contribute to heightened driver awareness but also play a pivotal role in facilitating the safe operation of autonomous vehicles. As a result of advances in technology, Mobile Mapping Systems (MMS) equipped with LiDAR units have emerged as effective tools capable of swiftly scanning road environments at normal driving speed while capturing exceptionally precise 3D point cloud data. Leveraging the geometric characteristics inherent to most traffic signs, such as linear and planar features, MMS LiDAR data have proven to be an ideal resource for identifying and evaluating the visibility of traffic signs (Zhang et al., 2019; Hirt et. al., 2022). Furthermore, MMS can also detect vegetation along the road right-of-way and assess the occlusion of signage caused by vegetation (Huang et al., 2017). Uncontrolled vegetation, as shown in Figure 1, can pose safety hazards for various reasons. Vegetation, weeds, brush, and tree limbs obscure or hinder driver's view of the road ahead, traffic control devices, approaching vehicles, wildlife, livestock, pedestrians, and bicycles (US Department of Transportation, 2008).
Due to advances in computer vision techniques such as semantic segmentation (Loce et al., 2013) and deep learning algorithms (Abduljabbar et al., 2019), researchers made significant progress in analyzing and enhancing signage visibility along transportation corridors (Choi et al., 2022). Semantic segmentation techniques have become increasingly important in the analysis of transportation corridors. By classifying the components of the road network into distinct objects, these techniques provide valuable insights for various applications, including road maintenance, autonomous driving, and transportation safety (Balado et al.,2019).

Figure 1. Illustration of a road sign (red circle) obscured by vegetation along the highway.

The aim of this study is to utilize MMS LiDAR data for traffic sign and vegetation detection which serves as a fundamental prerequisite for comprehensive signage visibility analysis. As illustrated in Figure 2, the proposed workflow encompasses two alternative strategies which are: 1) a geometric/morphological approach and 2) a learning-based approach. Initially, a geometric/morphological approach, namely Multi-Class Simultaneous Segmentation (MCSS) (Habib et al., 2016), will be employed to segment transportation corridor components based on the geometric features. For the learning-based semantic segmentation technique, the Super Point Graph (SPG) (Landrieu et al., 2018; Lin et al., 2022) is adopted in this study. Next, we compare how well morphological and learning-based strategies predict and detect signage and vegetation points. Overall, the objective of this research is to evaluate and compare the performance of morphological and learning-based strategies in identifying signage and vegetation points, analyzing the performance of semantic segmentation as well as evaluating the versatility of semantic segmentation in identifying various objects in the environment.

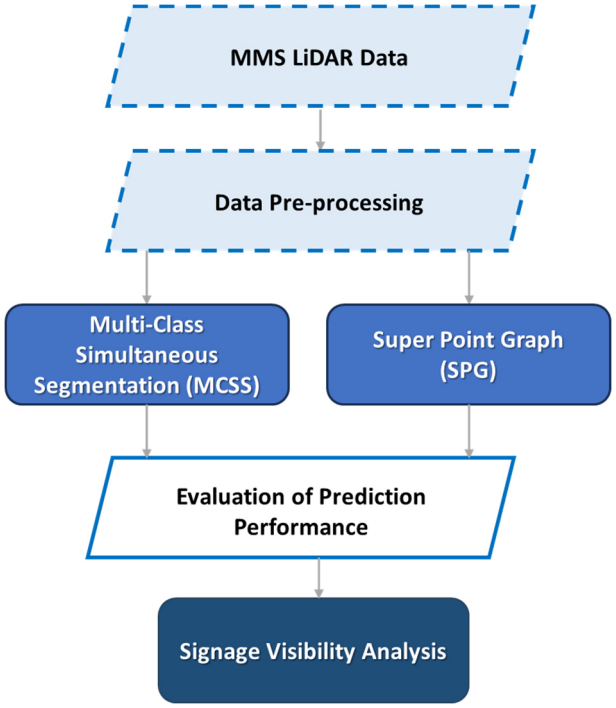

Figure 2. Proposed framework for comparative analysis of geometric/morphological and learning-based strategies for detecting signage occlusions.

2. MATERIALS AND METHODS

In this study, four datasets were acquired along a highway area using two Mobile Mapping Systems (MMS). These systems were developed by the Digital Photogrammetry Research Group (DPRG) at Purdue University. This section begins by introducing the developed Mobile Mapping Systems followed by a description of the acquired highway datasets.

2.1 Data Acquisition Systems

The MMS LiDAR datasets were acquired by a mapping-grade system, Purdue Wheel-based Mobile Mapping System-High Accuracy (*PWMMS-HA*), and a survey-grade system, Purdue Wheel-based Mobile Mapping System-Ultra High Accuracy (*PWMMS-UHA*) as shown in Figure 3. The *PWMMS-HA* is equipped with four LiDAR units (three Velodyne HDL-32E and one Velodyne VLP-16 High Resolution). Three FLIR Grasshopper cameras are mounted in the front-left, front-right, and rear of the vehicle. For direct georeferencing, an Applanix POS LV 220 unit is installed. The Velodyne HDL-32E has a range accuracy of ±2 cm, while the VLP-16 has a range accuracy of ±3 cm (Velodyne, 2023a; Velodyne, 2023b). The GNSS/INS unit has a post-processing positional accuracy of ±2 cm, along with an attitude accuracy of 0.020° for roll/pitch and 0.025° for heading (Applanix, 2023). On the other hand, the *PWMMS-UHA* is equipped with two LiDAR units (Riegl VUX-1HA and Z+F Profiler 9012). Two FLIR Flea2 FireWire cameras are mounted in the rear of the vehicle together with a NovAtel ProPak6 GNSS receiver for direct georeferencing. The range accuracy of the Riegl VUX-1HA and Z+F Profiler 9012 is ±5 mm and ±3 mm, respectively (Riegl, 2023; Z+F, 2023). The GNSS/INS unit on the *PWMMS-UHA* has a post-processing positional accuracy of ±1–2 cm, and its attitude accuracy is ±0.003° for pitch/roll and ±0.004° for heading (Novatel, 2023).

Figure 3. MMS LiDAR systems used in the study – *PWMMS-HA* (Top) and *PWMMS-UHA* (Bottom).

2.2 I-65 Highway Datasets

Four LiDAR datasets were acquired along the I-65 state highway (West Lafayette, Indiana, US) in two different regions of interest (ROI) as presented in Figure 4. The datasets for ROI 1 were acquired on February 23, 2021, during the leaf-off season, while the datasets for ROI 2 were acquired on June 8, 2020, during the leaf-on season. Further details regarding the acquired datasets are listed in Table 1.

Figure 4. Closer view of ROIs located along the I-65 state highway area (West Lafayette, Indiana, US).

Platform	ROI ID	Collection Date	*Number of Points	Dimension
PWMMS-HA	ROI 1	February 23, 2021	1,341,784	58 m × 97 m
	ROI 2	June 8, 2020	3,805,240	56 m × 246 m
PWMMS-UHA	ROI 1	February 23, 2021	663,275	58 m × 97 m
	ROI 2	June 8, 2020	1,665,884	56 m × 246 m

*The number of points is after outlier removal and distance-based down-sampling of 5 cm.

Table 1. Description of the four datasets located in two different ROIs acquired by the Mobile Mapping Systems.

3. METHODOLOGY

This section presents the methodology for signage visibility analysis using semantically-segmented features from morphological and learning-based approaches. The MMS LiDAR data were pre-processed for noise removal and distance-based downsampling of 5 cm. For point cloud segmentation, two techniques are adopted which are: 1) Multi-Class Simultaneous Segmentation (MCSS) and 2) Super Point Graph (SPG). For semantic annotation, the following classes are defined: 1) Bridge deck, guardrail, and beam/girder; 2) Bridge abutment and wing wall; 3) Bridge pier; 4) Man-made terrain; 5) Natural terrain; 6) Vegetation; 7) Buildings; 8) Scanning artifacts (e.g., moving vehicles and noise); and 9) Remaining hardscape, such as guardrails, traffic signs, light poles, etc.

As for the geometric/morphological approach, the point cloud is structured using an octree for MCSS (Habib et al., 2016). Then, Local Point Density (LPD)/Local Point Spacing (LPS) are estimated based on randomly selected portion of the entire point cloud and a user-defined local neighborhood size. The LPD/LPS estimation results of the selected points are used to represent the entire point cloud. Then, seed regions are generated from randomly selected seed points. Once the seed regions are defined, a Principal Component Analysis (PCA) is conducted to classify each seed region into planar, linear/cylindrical, or scattered neighborhood. The eigenvalues (λ_1,λ_2,λ_3) are sorted in a descending order ($\lambda_1 \geq \lambda_2 \geq \lambda_3$). Each point is evaluated to describe the local neighborhood by choosing the largest value in Equations 1 to 3 (Demantké et al., 2011). Next, a region-growing is conducted to group neighboring points that belong to the same feature type.

$$\text{Linearity:} \quad \frac{(\sqrt{\lambda_1}-\sqrt{\lambda_2})}{\sqrt{\lambda_1}} \tag{1}$$

$$\text{Planarity:} \quad \frac{(\sqrt{\lambda_2}-\sqrt{\lambda_3})}{\sqrt{\lambda_1}} \tag{2}$$

$$\text{Scattering:} \quad \frac{\sqrt{\lambda_3}}{\sqrt{\lambda_1}} \tag{3}$$

For planar and pole-like features, a Least Squares Adjustment (LSA) is conducted to assess the model-fitting quality as represented by its a-posteriori variance factor ($\hat{\sigma}^2$), which indicates the normal distance between the points within the seed region and the best-fitted model. Instead of starting the region-growing from the randomly established points, it starts from the best-fitted models with the minimum a-posteriori variance factor. Seed regions representing planar and pole-like features are sorted in ascending orders based on the estimated a-posteriori variance factor. During the region-growing process, the feature parameters are updated when a certain number of new points are introduced to the features. In this process, an outlier removal is conducted. Once all the seed regions are processed, a sequential region-growing segmentation is conducted for all non-segmented and rough regions. Lastly, a manual annotation process is conducted to assign labels to the derived segments.

For the learning-based approach, Super Point Graph (SPG) (Landrieu et al., 2018) is adopted for semantic segmentation. For computational efficiency, a pruning process is conducted by voxelization and representing each non-empty voxel with a single point in the pruned point cloud. An unoriented graph is established to represent the spatial structure of the point cloud. The adjacency graph is defined by finding the k-nearest neighboring points using a KD-tree structure for each point. For every point, a local neighborhood is determined by finding its k-nearest neighbors. Then a PCA analysis is conducted to evaluate the geometric characteristics for each local neighborhood as mentioned in Equations 1 to 3. In addition, verticality of the neighborhood is defined according to Equation 4.

$$[\hat{u}]_i \propto \sum_{j=1}^{3} \lambda_j \left| [u_j]_i \right|, \text{ for } i = 1,\ 2,\ 3 \text{ and } \|\hat{u}\| = 1 \tag{4}$$

Based on the geometric characteristics of local neighborhoods, the point cloud is partitioned into several regions using the l_0-cut pursuit algorithm (Landrieu et al., 2017a; Landrieu et al., 2017b). After geometric partitioning, super points are defined to represent each geometrically homogeneous partition. A Voronoi adjacency graph of the entire point cloud is defined to establish the adjacency relationship between super points. Once the super point graph is constructed, PointNet (Qi et al., 2017) is adopted to compute a descriptor for each super point. Here, handcrafted features are utilized in this stage which are: 1) geometric features (linearity, planarity, scattering, and verticality) and 2) trajectory features (2D distance to trajectory and relative height to ground). For the final stage, a contextual segmentation is conducted through a graph convolution to classify each super point based on its embedding as well as its surroundings within the super point graph. In addition, a quality control (QC) proposed by Lin et al. (2022) for road infrastructure is conducted in this work. Based on the trajectory information, the QC process refines the prediction for man-made terrain and scanning artifacts. In addition, predictions with low confidence levels are reported as "unclassified".

As for the signage visibility analysis, the occlusion rate is estimated by forming a pyramid using the signage boundary points as a base while the trajectory point is assumed to be the driver's viewpoint. Here, the vegetation intruding the pyramid is considered as occluding points. The occlusion rate computation, as presented in Equation 5, begins with projecting the occluding points onto the sign. Then, a 2D grid within the sign boundary is generated with a user-defined cell size which in this case is set as 0.1 m. After counting the occupied cells by occluding points, the occlusion rate is estimated as shown in Equation 5. In this work, we consider an occlusion rate that is under 10 % as acceptable for clear sign visibility.

$$\text{Occlusion Rate} = \frac{\text{Area of Occupied Grid Cells}}{\text{Bounding Area of the Sign}} \tag{5}$$

4. EXPERIMENTAL RESULTS

This section begins by presenting the comparative analysis of MCSS and SPG semantic segmentation results for detecting signage and vegetation points. Next, signage visibility analysis is conducted for *PWMMS-HA* and *PWMMS-UHA*.

4.1 Comparative Analysis of MCSS and SPG

In this section, a comparative analysis is conducted based on the prediction performance of MCSS and SPG. For SPG, the model was trained on *PWMMS-UHA* bridge datasets fine-tuned with the *PWMMS-HA* highway dataset with both driving directions. The reference data are generated through manual annotation of the point cloud. The performance is first qualitatively evaluated using reference data through visual inspection of the results for the four LiDAR datasets in different ROIs acquired by *PWMMS-HA* and *PWMMS-UHA*. Then, to quantitatively evaluate the performance of the approaches, the following metrics are computed using the reference data: 1) True Positive (TP); 2) False Positive (FP); 3) False Negative (FN); 4) Precision; 5) Recall; 6) F1-Score; and 7) Overall Accuracy. Here, precision, recall, F1-Score, and overall accuracy are derived as Equations 6 to 9.

Precision: $$\frac{TP}{(TP+TF)} \quad (6)$$

Recall: $$\frac{TP}{(TP+FN)} \quad (7)$$

F1-Score: $$2 \times \frac{Precision \times Recall}{Precision + Recall} \quad (8)$$

Overall Accuracy: $$\frac{TP}{Number\ of\ Points} \times 100 \quad (9)$$

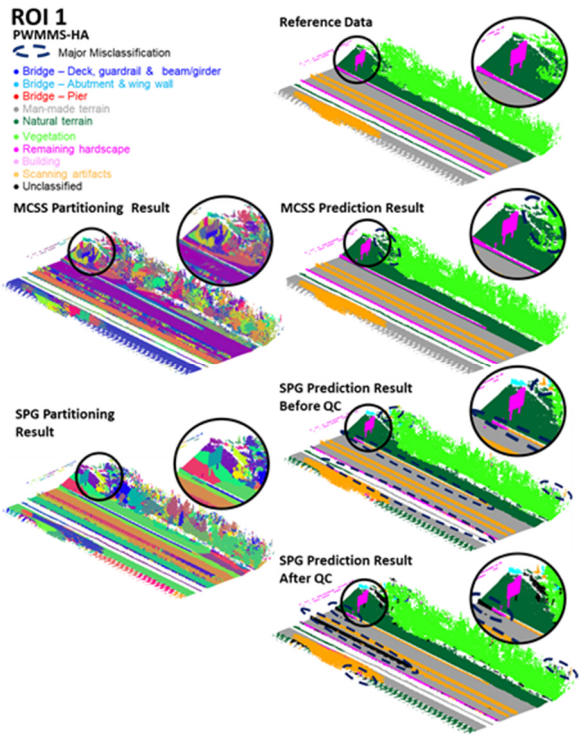

Figure 5. Comparison of partitioning results derived from MCSS and SPG (left). Evaluation of prediction performance for MCSS, SPG before QC, and SPG after QC (right) using reference data (top right), for ROI 1 from *PWMMS-HA*. Misclassifications are highlighted by black dashed circles.

Figure 5 shows the qualitative evaluation of the results for ROI 1 from PWMMS-HA, where some vegetation points in the MCSS prediction result were incorrectly labeled as natural terrain. Similarly, the SPG prediction result before QC misclassified vegetation points as scanning artifacts, remaining hardscape, natural terrain, and bridge components. Furthermore, some remaining hardscape points were misclassified as scanning artifacts and natural terrain. For natural terrain points, it was misclassified as man-made terrain or scanning artifacts. The quantitative evaluation of ROI 1 using MCSS as presented in Table 2, showed an overall accuracy of 99%. This indicates that the MCSS approach achieved a high level of accuracy in classifying the point cloud data in ROI 1. Tables 3 and 4 respectively, present a quantitative evaluation of SPG classification before and after QC. Before QC, the overall accuracy of the SPG approach was 91%. After QC, the accuracy showed a minimal improvement to 92%. This indicates that the QC had a negligible impact on enhancing the overall accuracy of the SPG prediction performance.

	TP	FP	FN	Prec.	Recall	F1-Score
Bridge – Deck	0.000	0.000	0.000	0.000	0.000	0.000
Bridge – Beam/girder	0.000	0.000	0.000	0.000	0.000	0.000
Bridge – Abutment & wing wall	0.000	0.000	0.000	0.000	0.000	0.000
Bridge – Pier	0.000	0.000	0.000	0.000	0.000	0.000
Man-made terrain	0.985	0.002	0.013	0.998	0.987	0.993
Natural terrain	0.941	0.045	0.013	0.954	0.986	0.970
Vegetation	0.982	0.005	0.013	0.994	0.987	0.991
Buildings	0.000	0.000	0.000	0.000	0.000	0.000
Remaining hardscape	0.942	0.041	0.016	0.958	0.983	0.970
Scanning artifacts	0.994	0.000	0.006	1.000	0.994	0.997
Overall accuracy	99%					

Table 2. Quantitative evaluation of MCSS classification results for ROI 1 from the *PWMMS-HA*.

	TP	FP	FN	Prec.	Recall	F1-Score
Bridge – Deck	0.000	1.000	0.000	0.000	0.000	0.000
Bridge – Beam/girder	0.000	0.000	0.000	0.000	0.000	0.000
Bridge – Abutment & wing wall	0.000	1.000	0.000	0.000	0.000	0.000
Bridge – Pier	0.000	1.000	0.000	0.000	0.000	0.000
Man-made terrain	0.841	0.122	0.037	0.874	0.958	0.914
Natural terrain	0.666	0.138	0.195	0.828	0.773	0.800
Vegetation	0.956	0.014	0.029	0.985	0.970	0.978
Buildings	0.000	0.000	0.000	0.000	0.000	0.000
Remaining hardscape	0.412	0.043	0.545	0.905	0.430	0.583

Scanning artifacts	0.861	0.119	0.020	0.878	0.977	0.925
Overall accuracy	91%					

Table 3. Quantitative evaluation of SPG classification results before QC for ROI 1 from the *PWMMS-HA*.

	TP	FP	FN	Prec.	Recall	F1-Score
Bridge – Deck	0.000	1.000	0.000	0.000	0.000	0.000
Bridge – Beam/girder	0.000	0.000	0.000	0.000	0.000	0.000
Bridge – Abutment & wing wall	0.000	1.000	0.000	0.000	0.000	0.000
Bridge – Pier	0.000	0.000	0.000	0.000	0.000	0.000
Man-made terrain	0.846	0.120	0.034	0.876	0.961	0.917
Natural terrain	0.679	0.123	0.198	0.847	0.774	0.809
Vegetation	0.962	0.013	0.024	0.987	0.975	0.981
Buildings	0.000	0.000	0.000	0.000	0.000	0.000
Remaining hardscape	0.428	0.040	0.533	0.915	0.445	0.599
Scanning artifacts	0.850	0.128	0.021	0.869	0.975	0.919
Overall accuracy	92%					

Table 4. Quantitative evaluation of SPG classification results after QC for ROI 1 from the *PWMMS-HA*.

As shown in Figure 6, in ROI 1 from the *PWMMS-UHA* dataset, the MCSS prediction result showed misclassifications where certain sections of natural terrain were incorrectly identified as vegetation, and vice versa. Similarly, the SPG prediction before QC showed misclassifications of natural terrain points as scanning artifacts and man-made terrain. Furthermore, there were incorrect classifications of remaining hardscape points as scanning artifacts, natural terrain, and bridge components. After the QC, misclassified areas were refined and reclassified as unclassified regions. Moreover, after QC, several points that were correctly classified were changed to unclassified points. Additionally, the F1-Score for the remaining hardscape class, which includes traffic signage, is 86%. As shown in Table 5, the overall accuracy is 98% for MCSS. The prediction performance metrics of SPG before and after QC are listed in Tables 6 and 7. The F1-Score for the remaining hardscape, which also includes traffic signs, was initially reported as 69%. However, after QC, it slightly decreased to 68%. In addition, there is no significant change in the F1-Scores for man-made terrain, natural terrain, remaining hardscape, and scanning artifacts after QC.

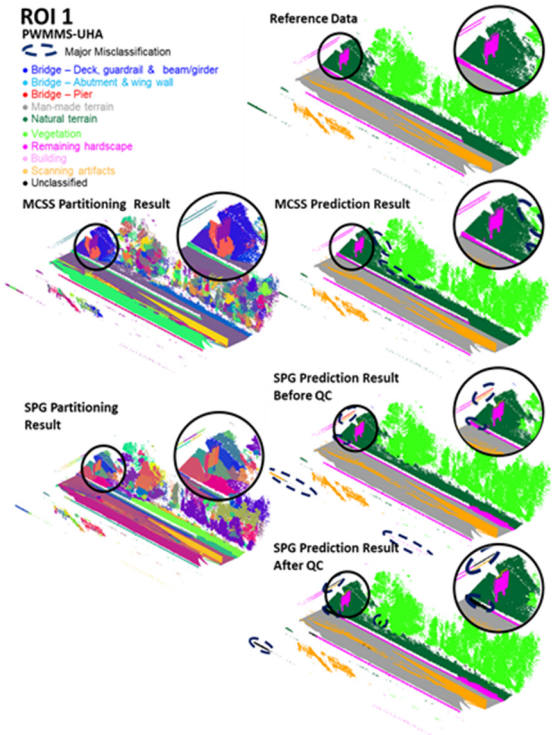

Figure 6. Comparison of partitioning results derived from MCSS and SPG (left). Evaluation of prediction performance for MCSS, SPG before QC, and SPG after QC (right) using reference data (top right), for ROI 1 from *PWMMS-UHA*. Misclassification is highlighted by black dashed circles.

	TP	FP	FN	Prec.	Recall	F1-Score
Bridge – Deck	0.000	0.000	0.000	0.000	0.000	0.000
Bridge – Beam/girder	0.000	0.000	0.000	0.000	0.000	0.000
Bridge – Abutment & wing wall	0.000	0.000	0.000	0.000	0.000	0.000
Bridge – Pier	0.000	0.000	0.000	0.000	0.000	0.000
Man-made terrain	0.978	0.000	0.021	0.999	0.979	0.989
Natural terrain	0.893	0.095	0.012	0.904	0.987	0.943
Vegetation	0.988	0.004	0.008	0.996	0.992	0.994
Buildings	0.000	0.000	0.000	0.000	0.000	0.000
Remaining hardscape	0.819	0.054	0.127	0.938	0.866	0.900
Scanning artifacts	0.996	0.000	0.003	0.999	0.997	0.998

Overall accuracy	98%

Table 5. Quantitative evaluation of MCSS classification results for ROI 1 from the *PWMMS-UHA*.

	TP	FP	FN	Prec.	Recall	F1-Score
Bridge – Deck	0.000	1.000	0.000	0.000	0.000	0.000
Bridge – Beam/girder	0.000	0.000	0.000	0.000	0.000	0.000
Bridge – Abutment & wing wall	0.000	0.000	0.000	0.000	0.000	0.000
Bridge – Pier	0.000	1.000	0.000	0.000	0.000	0.000
Man-made terrain	0.942	0.037	0.020	0.962	0.979	0.970
Natural terrain	0.778	0.041	0.181	0.950	0.811	0.875
Vegetation	0.985	0.005	0.010	0.995	0.990	0.993
Buildings	0.000	0.000	0.000	0.000	0.000	0.000
Remaining hardscape	0.537	0.359	0.104	0.600	0.838	0.699
Scanning artifacts	0.913	0.074	0.013	0.925	0.985	0.954
Overall accuracy	96%					

Table 6. Quantitative evaluation of SPG classification results before QC for ROI 1 from the *PWMMS-UHA*

	TP	FP	FN	Prec.	Recall	F1-Score
Bridge – Deck	0.000	1.000	0.000	0.000	0.000	0.000
Bridge – Beam/girder	0.000	0.000	0.000	0.000	0.000	0.000
Bridge – Abutment & wing wall	0.000	0.000	0.000	0.000	0.000	0.000
Bridge – Pier	0.000	0.000	0.000	0.000	0.000	0.000
Man-made terrain	0.943	0.036	0.021	0.963	0.978	0.971
Natural terrain	0.784	0.040	0.176	0.951	0.817	0.879
Vegetation	0.986	0.005	0.009	0.995	0.991	0.993
Buildings	0.000	0.000	0.000	0.000	0.000	0.000
Remaining hardscape	0.515	0.386	0.098	0.571	0.840	0.680
Scanning artifacts	0.929	0.060	0.012	0.940	0.988	0.963
Overall accuracy	96%					

Table 7. Quantitative evaluation of SPG classification results after QC for ROI 1 from the *PWMMS-UHA*

The same comparative analysis was conducted for ROI 2. Figure 7 shows the qualitative evaluation for results from the *PWMMS-HA* data. In the MCSS prediction result, some vegetation points were misclassified as natural terrain. Similarly, the SPG prediction result before QC had errors in classifying scanning artifacts as bridge components. Moreover, vegetation and natural terrain before QC were changed to unclassified after QC. As for the quantitative prediction performance, the overall accuracy of the MCSS result is 90%, while the SPG approach exhibit a lower accuracy of 72% both before and after QC.

The qualitative evaluation of the results from the *PWMMS-UHA* data is presented in Figure 8. MCSS prediction result showed misclassifications where certain vegetation points were incorrectly labeled as natural terrain. On the other hand, the SPG prediction results before QC misclassified natural terrain points as scanning artifacts and man-made terrain. The same quantitative analysis was conducted for ROI 2 from the *PWMMS-UHA*. The overall accuracy is 96% for the MCSS prediction result. Moreover, the overall accuracy for SPG after QC is 76% which showed an improvement from 74% before QC.

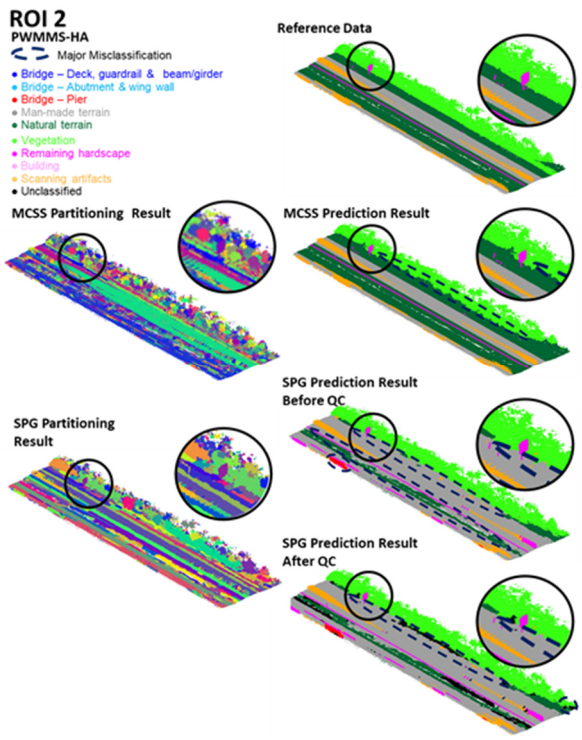

Figure 7. Comparison of partitioning results derived from MCSS and SPG (left). Evaluation of prediction performance for MCSS, SPG before QC, and SPG after QC (right) using reference data

(top right), for ROI 2 from *PWMMS-HA*. Misclassification is highlighted by black dashed circles.

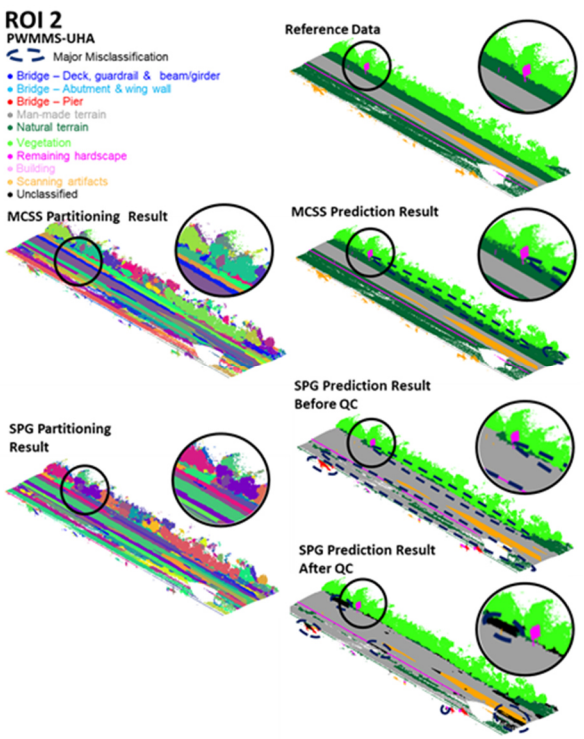

Figure 8. Comparison of partitioning results derived from MCSS and SPG (left). Evaluation of prediction performance for MCSS, SPG before QC, and SPG after QC (right) using reference data (top right), for ROI 2 from *PWMMS-UHA*. Misclassification is highlighted by black dashed circles.

4.2 Signage Visibility Analysis

In this study, signage visibility analysis is conducted based on ROI 2 which was acquired during the leaf-on seasons where there is a higher chance of the traffic sign being obscured by vegetation points. A comparison analysis of occlusion rates based on the distance from the sign to the driver's viewpoints for *PWMMS-HA* and *PWMMS-UHA* is conducted as shown in Figure 9. Based on the analysis, the occlusion rate for *PWMMS-HA* indicates that the drivers can only see the sign at a distance of 30 m. On the other hand, for *PWMMS-UHA*, the result indicates that the drivers can clearly see the sign at a distance of 50 m. The differences between the results from the two systems are caused by various numbers of onboard LiDAR sensors and scanning patterns for each type of the LiDAR sensors. Specifically, the point cloud from *PWMMS-HA* shows a more complete representation of the vegetation as illustrated in Figure 10, leading to a higher and more reliable occlusion rate. Based on the clear distance standard (US Department of Transportation, 2008), for a driver traveling at a speed of 60 mph, non-critical signs require to be visible from a minimum distance of 91 m. Therefore, the signage visibility analysis indicates that the sign is obscured by the vegetation in the presented example, posing safety hazards.

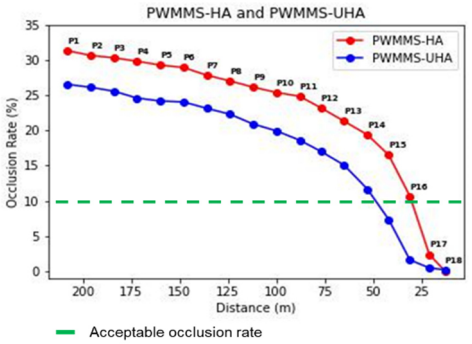

Figure 9. Comparison of occlusion rate based on the distance from the sign-to-driver's viewpoint for *PWMMS-HA* in red and *PWMMS-UHA* in blue.

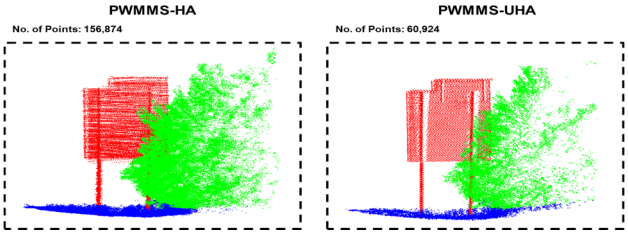

Figure 10. Comparison of LiDAR point clouds between *PWMMS-HA* and *PWMMS-UHA* for the sample traffic sign in ROI 2. The sign, vegetation points, and natural terrain are shown in red, green, and blue, respectively.

5. CONCLUSIONS

In terms of classification results, the MCSS outperformed the SPG approach overall. However, it is worth noting that the MCSS technique requires manual interaction throughout the classification process. The performance of SPG before QC exhibited a limited ability to accurately classify several classes, such as natural and man-made terrain. In addition, performing QC in the SPG approach did not significantly improve the classification performance. For the conducted signage visibility analysis, different occlusion rates were observed for a given sign from the two mobile mapping systems. Compared to *PWMMS-UHA,* the *PWMMS-HA* result produced a more reliable occlusion rate due to its ability to capture more complete point cloud for a better signage visibility analysis. Future study will focus on improving the overall accuracy for the deep learning-based approach as well as the QC. Furthermore, improving the quality of SPG geometric partitioning by integrating MCSS geometric segmentation as super points will be conducted.

ACKNOWLEDGEMENTS

This work was supported in part by the Joint Transportation Research Program administered by the Indiana Department of Transportation and Purdue University.
The authors would like to thank the Digital Photogrammetry Research Group (DPRG) members, especially Jidong Liu for their help throughout the data collections and analysis.

REFERENCES

Abduljabbar, R.; Dia, H.; Liyanage, S.; Bagloee, S.A. Applications of Artificial Intelligence in Transport: An Overview. Sustainability 2019, 11, 189. https://doi.org/10.3390/su11010189.

Applanix POSLV 220 Datasheet. Available online: https://www.applanix.com/downloads/products/specs/POS-LV-Datasheet.pdf (Accessed 12 July 2023).

Babić D., Babić D., Cajner H., Sruk A., Fiolić M. (2020) Effect of Road Markings and Traffic Signs Presence on Young Driver Stress Level, Eye Movement and Behaviour in Night-Time Conditions: A Driving Simulator Study. Safety 2020, 6(2), 24; https://doi.org/10.3390/safety6020024

Babić D., Babić D., Fiolic M., Ferko M. (2022) Road Markings and Signs in Road Safety. Encyclopedia 2022, 2(4), 1738-1752; https://doi.org/10.3390/encyclopedia2040119

Balado J, Martínez-Sánchez J, Arias P, Novo A. Road Environment Semantic Segmentation with Deep Learning from MLS Point Cloud Data. Sensors. 2019; 19(16):3466. https://doi.org/10.3390/s19163466.

Choi WC, Chong KS. (2022) Analysis of Road Sign-Related Factors Affecting Driving Safety with Respect to City Size. Appl. Sci. 2022, 12(19), 10163; https://doi.org/10.3390/app121910163

Demantké, J., Mallet, C., David, N. and Vallet, B., 2011. Dimensionality based scale selection in 3d lidar point clouds. The International Archives of the Photogrammetry, Remote Sensing and Spatial Information Sciences 38(Part 5), pp. W12. DOI:10.5194/isprsarchives-XXXVIII-5-W12-97-2011

Habib, A., & Lin, Y. J. (2016). Multi-class simultaneous adaptive segmentation and quality control of point cloud data. *Remote Sensing*, *8*(2). https://doi.org/10.3390/rs8020104

Heipke, C., Mayer, H., Wiedemann, C., & Jamet, O. (1997). Evaluation of automatic road extraction. International Archives of Photogrammetry and Remote Sensing, 32(3 SECT 4W2), 151-160.

Hirt, P. R., Holtkamp, J., Hoegner, L., Xu, Y., & Stilla, U. (2022). Occlusion detection of traffic signs by voxel-based ray tracing using highly detailed models and MLS point clouds of vegetation. International Journal of Applied Earth Observation and Geoinformation,114,103017.
https://doi.org/10.1016/j.jag.2022.103017

Huang, P., Cheng, M., Chen, Y., Luo, H., Wang, C., & Li, J. (2017). Traffic sign occlusion detection using mobile laser scanning point clouds. IEEE Transactions on Intelligent Transportation Systems, 18(9), 2364-2376. https://doi.org/10.1109/TITS.2016.2639582

Landrieu L., Obozinski G. Cut Pursuit: fast algorithms to learn piecewise constant functions on general weighted graphs. SIAM Journal on Imaging Sciences, 2017a, Vol. 10 (No. 4), pp. 1724-1766. DOI:10.1137/17M1113436

Landrieu, L.; Raguet, H.; Vallet, B.; Mallet, C.; Weinmann, M. A structured regularization framework for spatially smoothing semantic labelings of 3D point clouds. ISPRS J. Photogramm. Remote Sens. 2017b, 132, 102–118. DOI:10.1016/j.isprsjprs.2017.08.010

Landrieu, L. & Simonovsky M. (2018), Large-Scale Point Cloud Semantic Segmentation with Superpoint Graphs. IEEE/CVF Conference on Computer Vision and Pattern Recognition, Salt Lake City, UT, USA, pp. 4558-4567. DOI: 10.1109/CVPR.2018.00479

Lin, Y., & Habib, A., (2022) Semantic segmentation of bridge components and road infrastructure from mobile LiDAR data. ISPRS Journal of Photogrammetry and Remote Sensing, Volume 6,100023,ISSN2667-3932.
https://doi.org/10.1016/j.ophoto.2022.100023

Loce, R., Bernal E., Wu W., & Bala, R. (2013). Computer vision in roadway transportation systems: A survey. Journal of Electronic Imaging. 22. 10.1117/1.JEI.22. DOI:10.1117/1.JEI.22

Novatel, IMU-ISA-100C. Available online:. https://docs.novatel.com/OEM7/Content/Technical_Specs_IMU/ISA_100C_Performance.htm. (Accessed 12 July 2023).

Oscar Oviedo-Trespalacios O., Watson B., Jane A. Hinton J.A. (2019).The impact of road advertising signs on driver behaviour and implications for road safety: A critical systematic review, Transportation Research Part A: Policy and Practice,Volume 122, 2019. https://doi.org/10.1016/j.tra.2019.01.012

Qi, C. R., Su, H., Mo, K., & Guibas, L. J. (2017). Pointnet: Deep learning on point sets for 3d classification and segmentation. In Proceedings of the IEEE conference on computer vision and pattern recognition (pp. 652-660). https://doi.org/10.48550/arXiv.1612.00593

Riegl, VUX-1HA Datasheet. Available online: http://www.riegl.com/uploads/tx_pxpriegldownloads/DataSheet_VUX-1HA__2015-10-06.pdf (Accessed 12 July 2023).

Reiterer, A., Wäschle, K., Störk, D., Leydecker, A., & Gitzen, N. (2020). Fully automated segmentation of 2D and 3D mobile mapping data for reliable modeling of surface structures using deep learning. *Remote Sensing*, *12*(16). https://doi.org/10.3390/RS12162530

Smith, B. W. (2016). Automated driving policy. Road Vehicle Automation 3, 53-58.

US Department of Transportation, Federal Highway Administration (FHWA). (2008). Publication No. FHWA-SA-07-018: Office of Safety. Washington, DC.

Velodyne, HDL32E Datasheet. Available online: https://pdf.directindustry.com/pdf/velodynelidar/hdl-32e-datasheet/182407-676098.html (Accessed 12 July 2023a).

Velodyne, Puck Hi-Res Datasheet. Available online: https://velodynelidar.com/products/puck-hi-res/ (Accessed 12 July 2023b).

Vierhub-Lorenz, V., Kellner, M., Zipfel, O., Reiterer, A. (2022) A Study on the Effect of Multispectral LiDAR Data on Automated Semantic Segmentation of 3D-Point Clouds. Remote Sens. 2022, 14(24), 6349; https://doi.org/10.3390/rs14246349

Z+F, Profiler 9012. Available online: https://www.zofre.de/en/laser-scanners/2d-laser-scanner/z-f-profilerr-9012 (Accessed 12 July 2023).

Zhang, J., Zhao, X., Chen, Z., & Lu, Z. (2019). A review of deep learning-based semantic segmentation for point cloud. IEEE access, 7, 179118-179133. DOI:10.1109/ACCESS.2019.2958671

Zhang S., Wang C., Li L., Wen C., Yang C., Zhang Z., Li J. (2019), Automated Visual Recognizability Evaluation of Traffic Sign Based on 3D LiDAR Point Clouds. Remote Sens. 2019, 11(12), 1453; https://doi.org/10.3390/rs11121453